

Deterministic Assembly of Flexible Si/Ge Nanoribbons via Edge-Cutting Transfer and Printing for van der Waals Heterojunctions

Qinglei Guo, Miao Zhang, Zhongying Xue, Gang Wang, Da Chen, Ronggen Cao, Gaoshan Huang, Yongfeng Mei,* Zengfeng Di,* and Xi Wang

As the promising building blocks for flexible electronics and photonics, inorganic semiconductor nanomembranes have attracted considerable attention owing to their excellent mechanical flexibility and electrical/optical properties. To functionalize these building blocks with complex components, transfer and printing methods in a convenient and precise way are urgently demanded. A combined and controllable approach called edge-cutting transfer method to assemble semiconductor nanoribbons with defined width (down to submicrometer) and length (up to millimeter) is proposed. The transfer efficiency can be comprehended by a classical cantilever model, in which the difference of stress distributions between forth and back edges is investigated using finite element method. In addition, the vertical van der Waals PN (p-Si/n-Ge) junction constructed by a two-round process presents a typical rectifying behavior. The proposed technology may provide a practical, reliable, and cost-efficient strategy for transfer and printing routines, and thus expediting its potential applications for roll-to-roll productions for flexible devices.

1. Introduction

High-performance flexible electronics demonstrated on unconventional substrates such as plastic, elastomer, metal foil, and silk^[1–3] have been considered as an emerging technology, due to its versatile applications in displays, silicon

photonics, electronic sensory skins, energy harvesting, and structural health monitoring devices.^[4–9] Conventional materials for this purpose typically involve small-molecule organic and polymer materials,^[10] polycrystalline silicon,^[11] and single crystal inorganic semiconductors.^[12–15] And, simple and convenient methods^[16–23] have been widely developed and explored to meet the manufacturing requirement in micro- and nanoscale. Owing to their good mechanical flexibility and high carrier mobility, inorganic semiconductor nanomembranes (NMs)^[24,25] in forms of wires,^[26,27] ribbons,^[28] and meshes^[29] have attracted considerable attention as the promising building blocks for flexible electronics. Conventional approaches for the manufacturing of these building blocks with the feature size less than 1 μm generally involve high-resolution lithographic processing, even electron beam lithography^[5] and nanoimprint lithography^[30,31] are recently implemented for the dimension scaling of the building blocks. In addition, these nano- or microscaled elements, like wires^[23] and ribbons,^[32] can be produced by prudently anisotropic etching. However, such approach can only be applied to the crystalline semiconductors with superior anisotropy,

Dr. Q. Guo, Prof. M. Zhang, Dr. Z. Xue, Dr. G. Wang,
Dr. D. Chen, Prof. Z. Di, Prof. X. Wang
State Key Laboratory of Functional Materials
for Informatics
Shanghai Institute of Microsystem
and Information Technology
Chinese Academy of Sciences
Shanghai 200050, P. R. China
E-mail: zfdi@mail.sim.ac.cn

Dr. R. Cao, Prof. G. Huang, Prof. Y. Mei
Department of Materials Science
Fudan University
Shanghai 200433, P. R. China
E-mail: yfm@fudan.edu.cn

DOI: 10.1002/sml.201500505



e.g., Si, but not suitable for other semiconductors with poor anisotropy, e.g., Ge.^[33] Hence, an universal approach for the manufacturing micro/nanoscale building blocks for the applications of flexible electronics is still lacking.

Transfer printing^[34,35] as a versatile set of techniques can heterointegrate single crystalline semiconductor NMs on rigid substrate^[36] for heterointegrated photonic circuits,^[37,38] or on flexible substrate^[1–3] for electronics^[39] and photonics.^[5,40] Favored by van der Waals forces, micro/nanoscale NMs tethered to underneath substrates can merely maintain their lithographically defined geometries to some extent, but surely do not meet the high demand for the development of nanoscience and nanotechnology.^[41,42] To maintain the original spatial order, tethers and anchoring structures^[43–45] are introduced to fix the released micro/nanoscale elements in the defined positions by photolithography. However, although these special structures with designed tethers and anchors can well preserve the original spatial order during the transfer process via controlled fractures, the extra occupation of the source materials (e.g., silicon-on-insulator (SOI)) for tethers and anchors,^[43,44] the complex design for the “perimeter pedestal”,^[45] and the minimum dimension of the elements limited by the resolution of photolithography, impede the wide application of this technique.

Here, we develop a combined approach, including edge-cutting transfer (E-CT) to transfer Si/Ge nanoribbons to flexible substrates (e.g., polydimethylsiloxane (PDMS)) in a convenient and controllable way. The arrangement of Si/Ge nanoribbons exactly duplicates the same spatial order of the pattern predesigned on SOI or germanium-on-insulator (GOI) substrates. Herein, the correlation between the

geometry (width and thickness) of the transferred nanoribbons and the transfer efficiency has been investigated in detail. In addition, the stacked Si/Ge nanoribbons are demonstrated for vertical van der Waals PN junction.

2. Results and Discussions

Figure 1 presents a schematic illustration of the procedure to fabricate the flexible Si/Ge nanoribbon arrays by E-CT method. The process starts with a cleaned (100) XOI^[36] (SOI or GOI) wafer, as displayed in Figure 1a-i. Then the XOI wafer is patterned into strips with the length from micrometer to millimeter and several tens of micrometers in width by traditional photolithography and reactive ion etching (RIE) (Figure 1a-ii). The suspended Si/Ge nanoribbons can be released from the edges of the strips by the selective etching of buried oxide (BOX) layer with 5% HF solution (Figure 1a-iii), and the width of the suspended nanoribbons can be controlled by the etching time. The choice of 5% HF solution is due to its moderate and quite stable etching rate, which will be discussed later. Then a slap of cured PDMS is put into contact against the substrate, and then pulling away of the PDMS from the substrate with constant speed^[34,46] can cut the suspended Si/Ge nanoribbons off from the substrate in a controllable manner via fractures exactly at the fixed etching edge, as shown in Figure 1a-iv. Finally, the Si/Ge nanoribbon arrays are obtained by E-CT on flexible PDMS substrate as shown in Figure 1a-v (sketch) and Figure 1a-vi (optical image), where the white area is covered by the transferred silicon nanoribbon array. Thanks to the tether

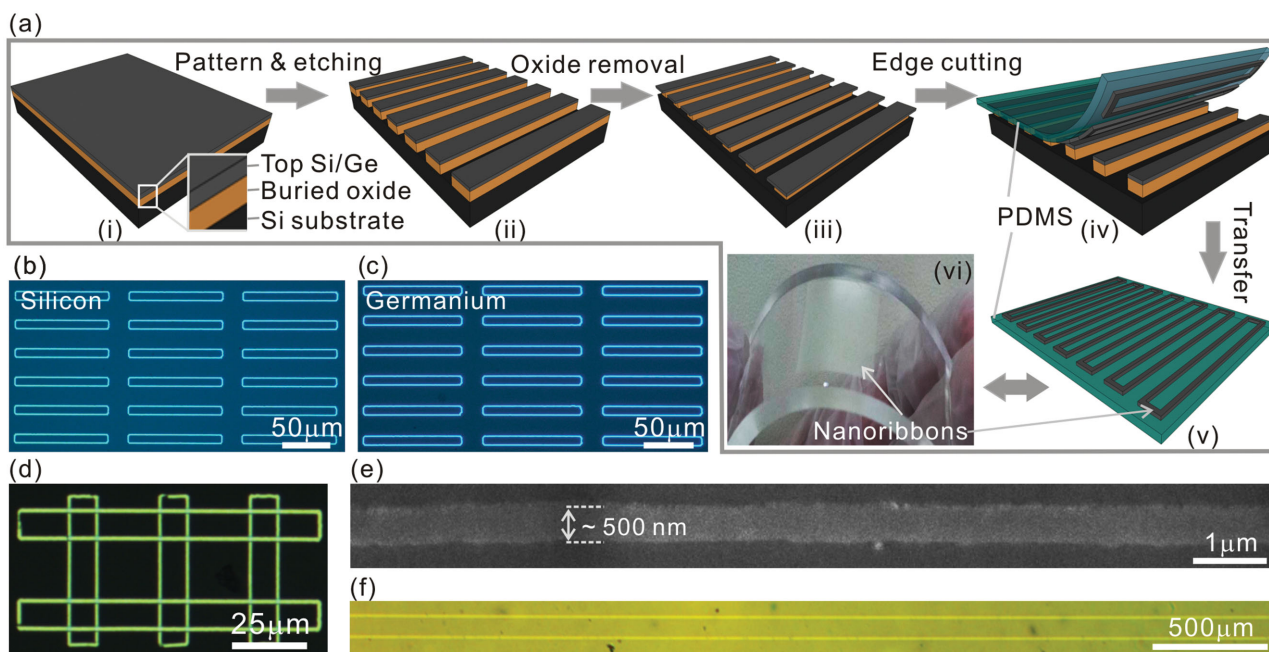


Figure 1. Si/Ge nanoribbons fabrication and characterization. a) Schematic illustration of the edge-cutting transfer (E-CT) process. The morphology of the as-transferred Si/Ge nanoribbons on PDMS substrate: b,c) Optical microscopy images of Si/Ge nanoribbons array on PDMS fabricated by E-CT. d) Optical microscopy image of stacked construction on PDMS with a nanoribbons pair fabricated by two-round E-CT processes. e) SEM of a Si nanoribbon on PDMS with the width of ≈ 500 nm. f) Optical microscopy image of an ultra-long Si nanoribbon on PDMS with a length more than 4000 μm .

and anchor-like effects provided by etching edge, the spatial order of the initial strips is completely replicated onto the transferred Si/Ge nanoribbon arrays on PDMS as displayed in Figure 1b,c. The edge cutting leads to the transfer of circumference of the patterned strip, i.e., ribbon shape, which appears in bright color in Figure 1b,c. The length of the ribbons can be easily tuned by the design of the starting strip.

The Si/Ge nanoribbons transferred on PDMS are further characterized by Raman spectroscopy. The corresponding Raman spectra shown in Figure S1b,d (Supporting Information) reveal the feature signals of transferred Si (Figure S1a, Supporting Information) and Ge (Figure S1c, Supporting Information) nanoribbons, respectively. With two rounds of E-CT processes under a perpendicular transfer direction, bilayered nanoribbons are stacked to form a crossbar structure on PDMS as shown in Figure 1d, where both layers are silicon nanoribbons transferred from SOI. Such approach could be deployed to integrate different materials to form heterojunctions under van der Waals force, e.g., Si/Ge heterojunction, as discussed later. The prominent advantage of E-CT process is that the width of the transferred nanoribbon is simply tuned by the corresponding etching time, but not restricted to the photolithography resolution limit. Even though the resolution limit of the traditional photolithography system used in our experiment is 2 μm , Si nanoribbon with the width of around 500 nm has been successfully transferred onto PDMS, as presented in Figure 1e. The aspect ratio of length to width of the transferred ribbons could reach more than 1000, even the thickness is only several tens of nanometer. Figure 1f shows ultra-long 50 nm thick Si nanoribbons with the width of 2 μm and 4000 μm in length on PDMS.

It is well-known that the single crystalline Si prefers to split along the crystal orientation [110] with the minimal total energy. However, there is no crystal-orientation-dependence for our E-CT method when transferring Si or Ge ribbons. An array of circular patterned Si mesas (diameter: 5 μm) without any preferential orientations are constructed by photolithography and RIE process as shown in Figure 2a. With the E-CT process, the contour edges of the designed circular patterns with certain width defined by the etching time are transferred, as exhibited in Figure 2b. And the inset shows the scanning electron microscopy (SEM) image of an array of as-transferred ring-like nanoribbon structures, which indicates that the proposed E-CT process is almost independent on the crystal orientation. Figure 2c shows a flower-like nanoribbon structure of Si on PDMS. The original pattern fabricated on SOI substrate (Figure S2, Supporting Information) can be completely transferred to PDMS with high accuracy in the spatial order. Also, an array of square nanoribbon structures of Si have been successfully transferred onto PDMS, as shown in Figure 2d. Nevertheless, some minor cracks exist in the transferred structures when the circumference of the transferred pattern is relatively long (Figure 2c). The cracking formation during the E-CT process will be discussed later.

In order to elucidate the physical mechanism for E-CT process, the beam theory^[47] is adopted for the edge-hanging structure (Figure 3a). For simplicity, the suspended Si

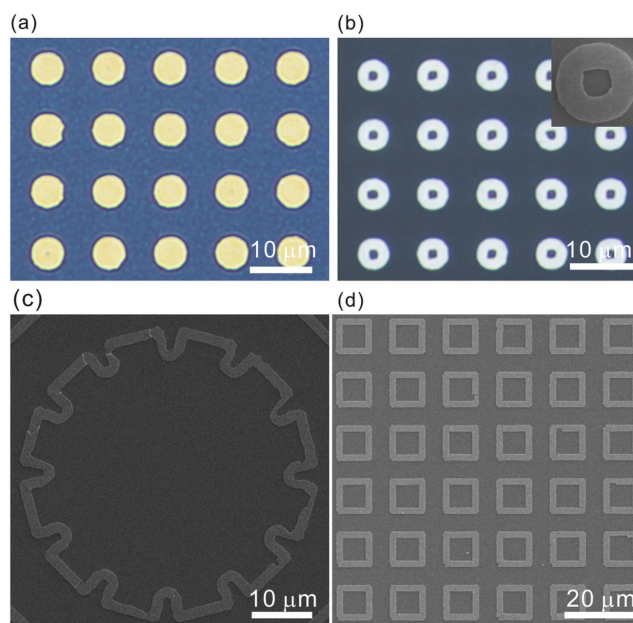


Figure 2. Optical and SEM images of the Si nanoribbons with unique patterns transferred by E-CT process. a) Optical microscopy image of the circle patterns fabricated on SOI wafer for the subsequent transfer. b) Optical microscopy image of ring-like Si nanoribbons on PDMS transferred from the patterns shown in (a) by E-CT process. c) SEM image of flower-like Si nanoribbon transferred on PDMS by E-CT process. d) SEM image of square Si nanoribbon transferred on PDMS by E-CT process.

nanoribbon is treated as a cantilever. Figure 3a schematically shows the sectional view of proposed cantilever beam model. The elastomeric PDMS contacts against a cantilever with a suspended edge, the adhesion force F is typically dominated by van der Waals interaction^[34] at the interface between PDMS and the cantilever. Such adhesion force is peeling-rate-dependent (that is constant at a certain peel rate), and provides uniformly distributed load (named q) for the cantilever beam to cut the nanoribbon off. F is proportional to the active surface area of the suspended nanoribbon, expressed as $F \propto l \times w$, where l and w are the length and width of the suspended nanoribbon, respectively, and q is defined as $q = F/w$. For clarity, the etching edges are classified into two kinds, “forth” edge and “back” edge. For the “forth” edge, the angle θ depicted in Figure 3a exceeds 90°, while the corresponding θ is less than 90° for the “back” edge. Therefore, when peeling off the ribbons from a rectangle pattern, the “forth” edge is always cut off prior to the “back” edge. To simplify the theoretical analysis, θ_{forth} and θ_{back} denote the angle θ for the “forth” edge and the “back” edge, respectively. Meanwhile, the “forth” edge and the “back” edge are both along the longer edge of transferred rectangle structure and the sum of θ_{forth} and θ_{back} equals to 180°. For the “forth” edge, the uniformly distributed load q can be disintegrated into the vertical component $q_v = q \sin \theta_{\text{forth}}$ and the horizontal component $q_h = q \cos \theta_{\text{forth}}$, which are directly exerted on the top surface of the NM, so the dominant stress distribution in the cantilever beam is

$$\sigma_{\text{forth}}(q, x) = \sigma_{\text{qv}}(q \sin \theta_{\text{forth}}, x) + \sigma_{\text{qh}}(q \cos \theta_{\text{forth}}, x) \quad (1)$$

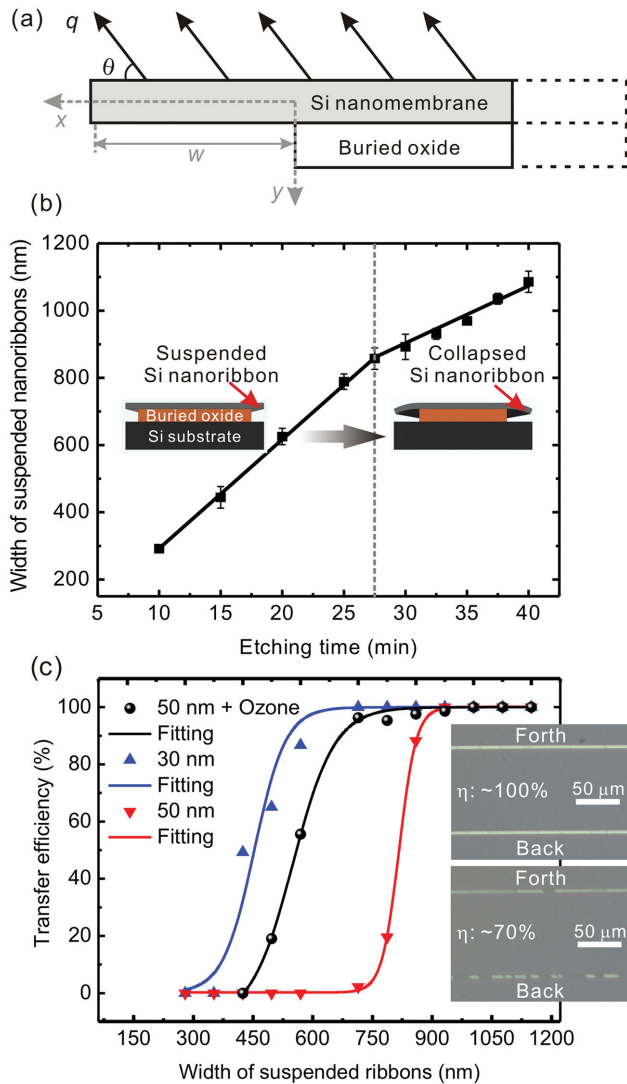


Figure 3. Theoretical model and transfer efficiency curves versus the width of the suspended Si NMs. a) Schematic illustration of cantilever beam model for E-CT process. b) Width of suspended Si nanoribbons versus HF etching time. c) Transfer efficiency curves versus the width of the suspended Si nanoribbons with the thicknesses of 30 and 50 nm under weak generalized adhesion caused by van der Waals force and strong adhesion generated by bridging siloxane –Si–O–Si– bonds, respectively. The transfer efficiency data are fitted using Boltzmann function.

where $\sigma_{\text{forth}}(q, x)$ is the stress distribution along x -direction during E-CT process. $\sigma_{\text{qv}}(q \sin \theta_{\text{forth}}, x)$ and $\sigma_{\text{qh}}(q \cos \theta_{\text{forth}}, x)$ denote the stress induced by vertical component and horizontal component of the external load, respectively. According to the beam theory,^[47] $\sigma_{\text{qv}}(q \sin \theta_{\text{forth}}, x)$ can be calculated as (further details are discussed in the Supporting Information)

$$\sigma_{\text{qv}}(q \sin \theta_{\text{forth}}, x) = \frac{6(q \sin \theta_{\text{forth}}) \times (w - x)^2}{t^3} y \quad (2)$$

where t denotes the thickness of the NM inherited from the starting SOI, and y is the distance from the center plane of the nanoribbon. Meanwhile, the horizontal component q_{h}

which directly acts on the top surface of the nanoribbon plays a role of compression on the top surface, and the corresponding tension can be exerted on the bottom surface of the nanoribbon. As a result, the upper portion of the nanoribbon is compressive, while the lower portion is tensile.

According to the discussion above, $\sigma_{\text{qh}}(q \cos \theta_{\text{forth}}, x) < 0$ corresponds to the upper portion ($y < 0$), while $\sigma_{\text{qh}}(q \cos \theta_{\text{forth}}, x) > 0$ corresponds to the bottom portion ($y > 0$). Substituting Equation (2) into Equation (1), the coordinate of the maximal stress in the cantilever beam for “forth” edge is $x = 0$, $y = \pm t/2$, and expressed as (further details are discussed in the Supporting Information)

$$\sigma_{\text{forth}}(q, x) = \pm \frac{3(q \sin \theta_{\text{forth}}) \times w^2}{t^2} + \sigma_{\text{qh}}(q \cos \theta_{\text{forth}}, x) |_{x=0, y=\pm \frac{t}{2}} \quad (3)$$

For the “back” edge, the similar result is obtained

$$\sigma_{\text{back}}(q, x) = \pm \frac{3(q \sin \theta_{\text{back}}) \times w^2}{t^2} + \sigma_{\text{qh}}(q \cos \theta_{\text{back}}, x) |_{x=0, y=\pm \frac{t}{2}} \quad (4)$$

If the consequent stress for either “forth” edge or “back” edge exceeds the critical mechanical strength of Si nanoribbon, the corresponding Si nanoribbon can be cut off and transferred to PDMS substrate. The proposed E-CT method is partly similar to mechanical exfoliation technique for graphene synthesis invented by Novoselov et al.,^[48] as the adhesive force initiates the layer transfer in both two approaches. However, other than the weak van der Waals force which needs to be overcome during the mechanical exfoliation, the Si–Si covalent bonds at the cutting edge of the suspended Si nanoribbon should be fractured when transferring Si nanoribbon by the E-CT process. Equations (3) and (4) suggest that the stress values for both “forth” and “back” edges increase proportionately to w^2 while inversely to t^2 . Considering that θ_{forth} and θ_{back} are complementary, the first items for $\sigma_{\text{forth}}(x)$ and $\sigma_{\text{back}}(x)$ have the same value, and the substantial difference between $\sigma_{\text{forth}}(x)$ and $\sigma_{\text{back}}(x)$ is the second item caused by the horizontal component of the uniformly distributed load acting on the suspended Si nanoribbon. For “forth” edge, as discussed previously, the second item $\sigma_{\text{qh}}(q \cos \theta_{\text{forth}}, x) < 0$ at the top region ($y < 0$) and $\sigma_{\text{qh}}(q \cos \theta_{\text{forth}}, x) > 0$ at the bottom ($y > 0$). While for the “back” edge, the second item $\sigma_{\text{qh}}(q \cos \theta_{\text{back}}, x)$ reveals opposite behavior but its absolute value is same as that of the “forth” edge, because the horizontal load components are opposite for “forth” and “back” edges. As a result, the absolute value of the stress which applies on the suspended ribbon for “forth” edge is much greater compared to “back” edge, and thus resulting in the ease cutting of “forth” edge.

According to the beam theory, a representative pattern, i.e., strips with a series of widths of suspended edges, is chosen to analyze the transfer efficiency of E-CT process. The width of the suspended ribbons can be tuned by HF etching time. It is observed that the width of the suspended Si

nanoribbon increases linearly with the etching time initially, and the slope of the fitting line represents the etching rate, as shown in Figure 3b. When the width becomes broad, the suspended Si nanoribbon is prone to collapse, thus impeding the further etching of buried oxide layer by HF solution. Therefore, the etching rate will decrease accordingly, as evident by the reduced slope of the fitting line.

The transfer efficiency η is defined as $\eta = S/S_0$, where S_0 is the area of the suspended Si nanoribbons prior to PDMS peeling and S is the area of the retrieved Si nanoribbons on PDMS. In Figure 3c, two representative images corresponding to the entire transfer state with the transfer efficiency being nearly 100% and the partial transfer state with the transfer efficiency being around 70% are shown. For the partial transfer state, it further shows that the transfer efficiency of the suspended Si nanoribbons with “forth” edge is much higher than that of “back” edge, which agrees well with the theoretical analysis [Equations (3) and (4)].

For 50 nm thick suspended Si nanoribbons, the transfer efficiency η versus the nanoribbon width w is obtained by analyzing optical microscope images (Figure S3a, Supporting Information) and the statistical results are displayed in Figure 3c with the red discrete solid triangle. During the incubation period, the suspended Si nanoribbons start to form as the etching of BOX proceeds. However, due to the relatively narrow width, the adhesion force F , which is proportional to the active surface area of the suspended nanoribbon, is inadequate to induce the cutting and the transfer of Si nanoribbon. As a result, the transfer efficiency curve undergoes a flat segment with the transfer efficiency value of 0%. As the width of suspended Si nanoribbon reaches 750 nm, the transfer efficiency starts to increase in a quadratic manner against the width until saturates at 100% as the width exceeds 950 nm. The obtained transfer efficiency curve versus the width of Si nanoribbon agrees with the beam theory in which the stress values for both “forth” edge and “back” edge increase proportionately to w^2 .

In addition to the stress dependence on the width of Si nanoribbon, the stress distribution appears inverse to t^2 , as suggested by the theoretical analysis. To examine the influence of thickness of Si nanoribbon on the transfer efficiency, the transfer behavior of Si nanoribbons with the reduced thickness of 30 nm has been explored (Figure S3b, Supporting Information), as displayed in Figure 3c with the blue discrete solid triangle. As predicted by the beam theory, the transfer efficiency is considerably enhanced when the Si nanoribbon thickness is reduced from 50 to 30 nm. Furthermore, many studies have indicated that the van der Waals interactions are able to alter the mechanical properties of low-dimensional materials.^[49–51] As the thickness of Si nanoribbon continues to shrink, the variation of mechanical properties induced by van der Waals interactions may also be responsible for the improvement of transfer efficiency. Hereinafter, only 30 nm thick Si NMs have been investigated unless otherwise specified.

Besides the proportional correlation with w^2 and the inverse relationship to t^2 , the stress exerted on the suspended Si nanoribbon is also proportional to the external uniform distributed load, q , which is determined by the interactions

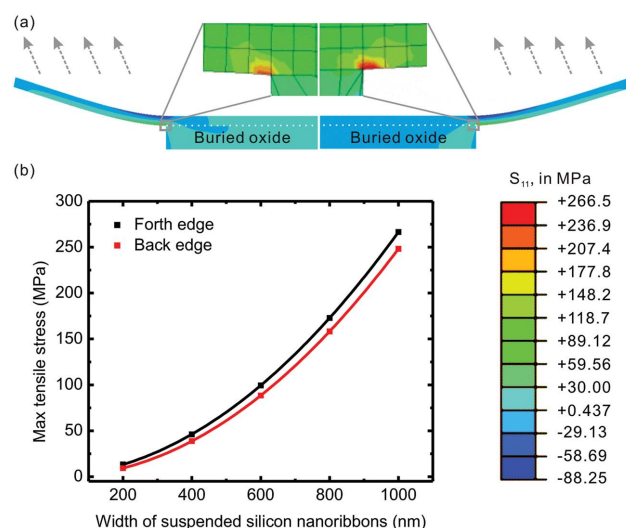


Figure 4. FEM calculations of stress distribution in suspended Si nanoribbons during the E-CT process. a) Deflection and stress distribution (S_{11}) of “forth” edge and “back” edge. b) Maximum of S_{11} tensile stress as a function of the width of suspended Si nanoribbons for “forth” edge and “back” edge, respectively.

between PDMS and the suspended Si nanoribbons. Without any intentional treatment, the surface of the PDMS is hydrophobic and dominated by $-\text{OSi}(\text{CH}_3)_2\text{O}-$ groups, and therefore, the interactions should be relatively weak and are mainly contributed by van der Waals force. It is known that the ozone is capable of converting the $-\text{OSi}(\text{CH}_3)_2\text{O}-$ groups on the hydrophobic PDMS surface into $-\text{O}_n\text{Si}(\text{OH})_{4-n}$ functionalities.^[14] The $-\text{O}_n\text{Si}(\text{OH})_{4-n}$ groups are prone to react with the $-\text{Si}-\text{OH}$ groups on suspended Si nanoribbons to form the strong siloxane linkages ($-\text{O}-\text{Si}-\text{O}-$). Thus, the uniformly distributed external load q will be considerably enhanced as the PDMS is pretreated by ozone. Accordingly, the transfer efficiency of the suspended Si nanoribbons on the ozone-treated PDMS is significantly improved, as evident by the distinct “down shift” exhibited in Figure 3c. Besides the chemical modification of PDMS substrate, the transfer efficiency of the suspended Si nanoribbons is also influenced by the peeling direction of PDMS relative to the host strips (Figure S4, Supporting Information).

In order to elucidate the physical mechanism underlying the transfer process, the finite element modeling (FEM) simulation using ABAQUS is performed, and the material parameters are chosen according to the values reported in the literatures.^[52,53] In the FEM simulation, S_{11} denotes the component of the stress tensor that along the x -axis, as shown in **Figure 4a**. The tensile component^[54] of S_{11} stress is believed to be responsible for the cutting and transfer behavior of the suspended Si nanoribbon from the SOI onto PDMS in this study. In the FEM simulation, a uniform pressure (0.1 MPa) is assumed to be exerted on the suspended Si nanoribbons and the tilted angle for “forth” edge and “back” edge are simplified as $\theta_{\text{forth}} = 135^\circ$ and $\theta_{\text{back}} = 45^\circ$, respectively. Figure 4a shows the distribution of S_{11} in a 1 μm wide suspended Si nanoribbon with both “forth” edge (right) and “back” edge (left). As predicted by the beam theory, the compressive stress distributes in the upper portion of the

nanoribbons, while the lower portion is in tension. Furthermore, the maximum tensile stress of S_{11} , which is crucial for the cutting behavior of the Si nanoribbons, is observed to distribute along the etching edge [the position corresponds to $x = 0$ and $y = t/2$ in Equations (3) and (4)]. Figure 4b shows the maximum value of tensile stress for “forth” edge and “back” edge with different widths. It suggests that, for the suspended Si nanoribbons with the same physical dimension, the maximum value of tensile stress for “forth” edge is larger than that for “back” edge. Therefore, the suspended Si nanoribbons with “forth” edges seem more prone to be cut and transferred than those with “back” edges, which is in agreement with the experimental observation and the beam theory. In addition, for either “forth” edge or “back” edge, the maximum stress increases in a quadratic manner as the width of Si nanoribbon increases. However, as the thickness of Si nanoribbon increases, the maximum stress of S_{11} shrinks rapidly (not shown).

Even the ultra-long Si nanoribbons with 100% transfer efficiency have been successfully obtained by tuning their thickness and width as suggested by the beam theory and FEM, it is still difficult to eliminate the formation of discrete cracks, which are frequently observed along the Si nanoribbons (Figure S5, Supporting Information). In order to investigate the formation of the cracks in the as-transferred Si nanoribbons by E-CT process, seven pairs of Si nanoribbons, which consist of both “forth” edge and “back” edge, have been transferred onto PDMS, and the length of ribbons is designed as long as 8 mm. After analyzing the numbers of cracks by optical microscopy, the crack densities of the ribbons for both “forth” edge and “back” edge are summarized in **Figure 5a**. It is shown that the “forth” edge has less cracks compared with “back” edge, indicating the average length of the ribbon segment between two adjacent cracks for “forth” edge is larger than that of “back” edge. With the statistical analysis, it is found that the average length of the ribbon segment for “forth” edge is about 250 μm , while, it decreases to 100 μm for “back” edge. Furthermore, the crack density of transferred Si nanoribbon is closely correlated to the peeling direction of PDMS relative to the host strips, as discussed in Figure S6 (Supporting Information).

Fracture theory developed by Inglis^[55] suggests that cracks are always formed when the stress concentration reaches the certain critical level. Cracks formed in the ductile material like PDMS are stable and grow slowly, while in the brittle material like Si or Ge, cracks are unstable and will continue spontaneously to induce the complete fracture. It should be noted that the bending of ductile PDMS stamp during the E-CT process is easy to generate the focal point of stress in the Si nanoribbon attached, where the cracks initiate as the Si nanoribbons are relatively robust.^[56] Cracks in Si, which are controlled by surface tensile strain, have been considered as one of the failure modes in flexible electronics, as demonstrated by Rogers' group.^[57] Thus, for the potential applications in the field of flexible electronics, the crack-free Si nanoribbons transferred on the flexible substrate are requested. In order to eliminate the possible cracks in the transferred Si nanoribbons, we adjust the photolithography pattern size of the starting Si strips and ensure the length is

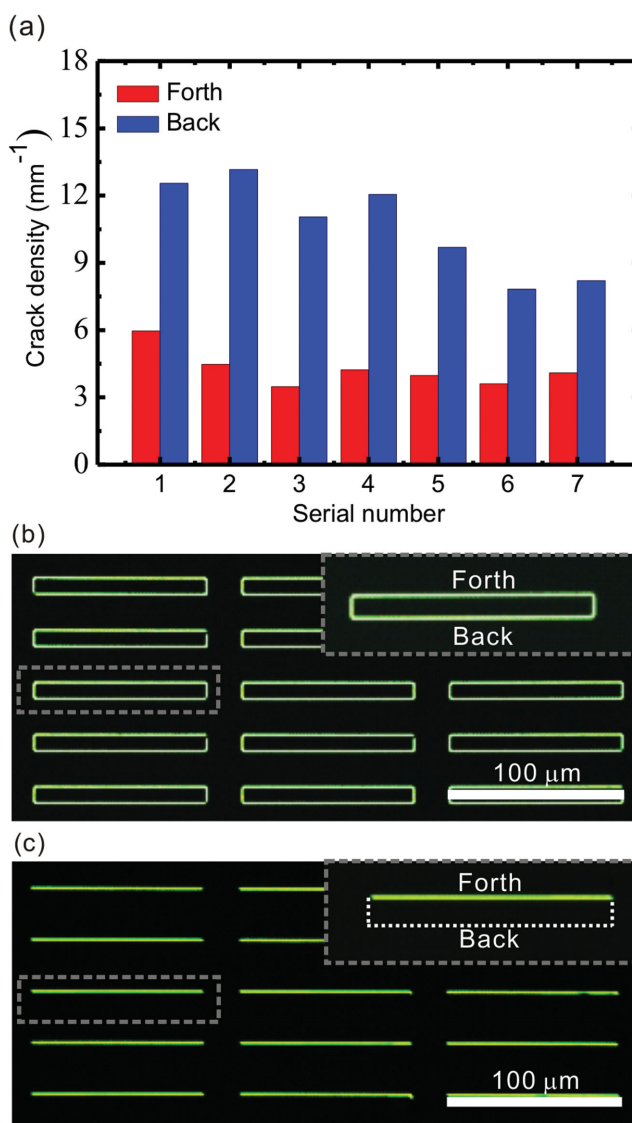


Figure 5. Cracking behavior for “forth” edge and “back” edge. a) Statistical results of crack densities for “forth” edge and “back” edge of a series of strips. b) Optical microscope images of crack-free Si nanoribbons on PDMS consisting of both “forth” edge type and “back” edge type. The width and the length are ≈ 1100 nm and ≈ 100 μm , respectively. c) Optical microscopy images of the crack-free Si nanoribbons on PDMS consisting of only the “forth” edge type. The width and the length are ≈ 800 nm and ≈ 100 μm , respectively.

less than or equal to the average segment length obtained in Figure 5a. Figure 5b shows the optical microscope image of 100 μm long Si nanoribbons transferred on PDMS by E-CT process. Since the designed length of 100 μm is relatively smaller than the average segment length, no crack is observed along the whole transferred Si nanoribbon arrays. When the width of Si nanoribbons is modulated as 1100 nm or above, the pair of Si nanoribbons including both “forth” edge and “back” edge can be completely transferred onto PDMS, and the spatial order is duplicated accordingly. Since the tensile stress exerted on Si nanoribbon with “forth” edge is always larger than that of “back” edge as suggested by the FEM simulation, it is feasible to transfer the Si nanoribbons pair or only the “forth” edge by tuning the width of Si

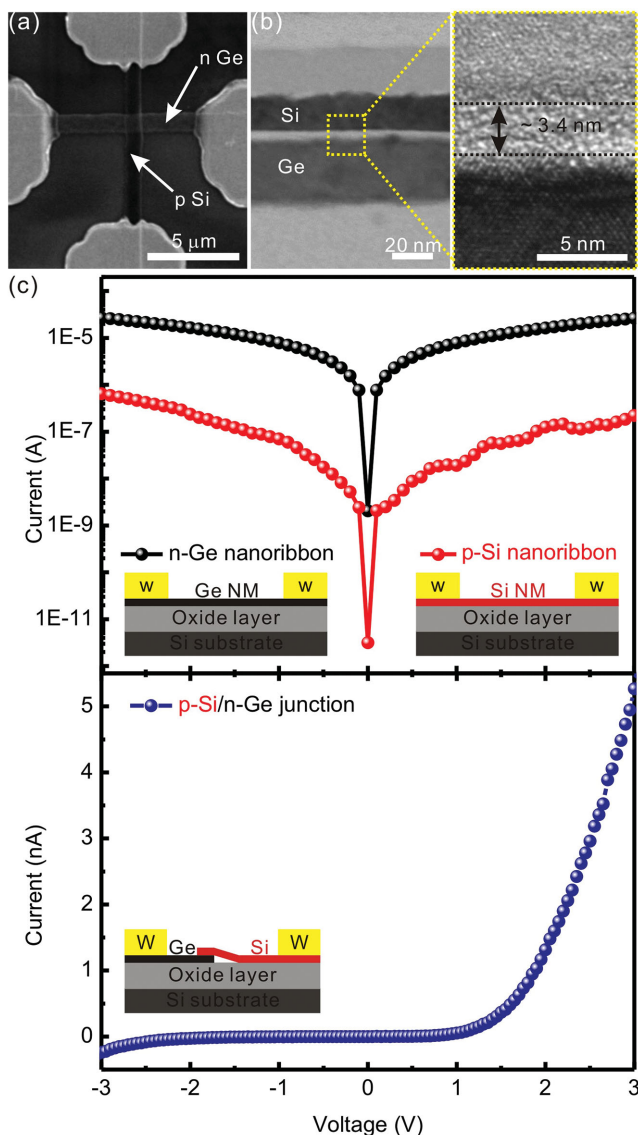


Figure 6. Crossed van der Waals PN junctions. a) SEM image of the van der Waals p-Si/n-Ge PN junction on SiO₂/Si substrate. b) TEM image showing Si/Ge interface of van der Waals p-Si/n-Ge PN junction. c) *I*-*V* characteristics of p-Si nanoribbon, n-Ge nanoribbon, and the van der Waals p-Si/n-Ge PN junction, respectively.

nanoribbons. In Figure 5c, only Si nanoribbons with “forth” edge have been transferred when the width decreases from 1100 to 800 nm.

Crack-free nanoribbons achieved by E-CT process can act as the essential building blocks for flexible electronic devices, which can be further functionalized by the integration. As illustrated in **Figure 6a**, the van der Waals heterojunction consisting of a p-type Si nanoribbon perpendicularly stacked on an n-type Ge nanoribbon is fabricated on a (300 nm) SiO₂/Si substrate by two-round E-CT processes. The SEM image shows the junction area is about 1 μm², and tungsten (W) contacts (100 nm thick) are deposited on the Si and Ge nanoribbons by focused ion beam (FIB) deposition. Figure 6b shows a transmission electron microscopy (TEM) image of Si/Ge van der Waals heterojunction. TEM image displays that single-crystalline Si nanoribbon distinctly

stacks on a single-crystalline Ge layer with a ≈3.4 nm thick intermediate layer, and no detectable void is observed along the intermediate layer. And the energy dispersive X-ray spectroscopy (EDX) result (Figure S7, Supporting Information) suggests that intermediate layer is assumed to consist of the native oxide of Si and Ge. Without any postfabrication treatment, *I*-*V* characteristics of the junction suggest that the metal–nanoribbon contacts for both p-Si and n-Ge are Schottky type, as displayed in Figure 6c. And the slight asymmetry in *I*-*V* behavior can be understood by different Schottky contacts at the source and drain.^[58,59] However, as p-Si nanoribbon is integrated with n-Ge nanoribbon to form the van der Waals PN heterojunction,^[60,61] a well rectifying behavior is obtained, as exhibited in Figure 6c. Therefore, the existence of the ultra-thin intermediate oxide layer may not affect the rectification characteristic of the junction.^[62] However, the large resistance between Si/Ge junction^[63] due to the presence of intermediate oxide layer is believed to be responsible for the relatively low current at forward bias. The well-behaved rectification characteristic implies that the achieved van der Waals PN heterojunction by E-CT technique is very promising to be integrated as the basic element for flexible electronic applications.

3. Conclusions

In summary, crack-free Si and Ge nanoribbons on PDMS substrate, which are the essential building blocks for flexible electronic devices, have been achieved by the proposed E-CT process. Since the width of the transferred Si/Ge nanoribbon is determined by the etching time, E-CT process is capable of delivering the nanoribbon with the width exceeding the resolution limit of photolithography utilized. The beam theory and the FEM modeling suggest the stress in ribbon increases proportionately to the square of its width while inversely to the square of its thickness, and the maximum tensile stress, which guides the cutting behavior of the Si nanoribbon, concentrates along the etching edge. With the appropriate design of the photolithography pattern of the starting strips, crack-free Si/Ge nanoribbons can be achieved successfully. As the building blocks for the flexible electronic devices, crack-free Si/Ge nanoribbons are further integrated into a van der Waals PN heterojunction, in which the well rectifying behavior is demonstrated. Our study may provide a simple and convenient method for the accurate assembly of micro/nanoscale semiconductor NMs (e.g., Si NMs or Ge NMs), which are expected to be further implemented into flexible electronic applications.

4. Experimental Section

Transfer Method: p-type Si nanoribbons were deviated from (100) SOI wafers (top Si layer: 30 or 50 nm, BOX layer: 120 nm), while n-type Ge nanoribbons were obtained from (100) GOI wafer (top Ge layer: 50 nm). And all the wafers were patterned by conventional photolithography using AZ 1500 photoresist and etched by RIE using SF₆ plasma (for Ge etching, O₂ plasma was also introduced and the volume ratio for SF₆ and O₂ is 100:1). After

the photoresist was dissolved by acetone, the patterned SOI (GOI) wafer was dipped into 5% HF solution to form suspended Si (Ge) nanoribbons tethering on the edge of the patterned strips. A cured PDMS stamp was put conformal contact against the SOI (GOI) wafer, then pulling it back to cut and transfer the suspended Si (Ge) nanoribbons on PDMS substrate with a constant rate.

Ozone Treatment of PDMS Substrates: Cured PDMS slabs with the thickness of ≈ 3 mm were rinsed with alcohol and deionized water, and dried using nitrogen gas blowing. In order to generate strong adhesion, the PDMS substrates were exposed to UV radiation and ozone to modify the surface for 1 min.

Fabrication of van der Waals PN Heterojunction: An ordered array of van der Waals PN heterojunctions was fabricated by two-round E-CT processes. After the transfer of P-doped n-type Ge nanoribbon array with thickness of 50 nm on PDMS stamp by the first round E-CT process, the PDMS was used as a stamp to print the nanoribbon arrays onto a (300 nm) SiO_2/Si substrate. The second round E-CT process was performed to transfer a B-doped p-type Si nanoribbon array with the length of 50 μm on PDMS, and then the Si nanoribbon array was printed onto the former n-Ge nanoribbon array to form the van der Waals PN heterojunction array. The orientation of the Si nanoribbon was set to be perpendicular to the Ge nanoribbon. The 100 nm thick W contact pads were deposited onto the terminals of the formed van der Waals PN heterojunction by FIB deposition. *I-V* measurements were performed on a probe station at room temperature.

Supporting Information

Supporting Information is available from the Wiley Online Library or from the author.

Acknowledgements

This work was financially supported by Creative Research Groups of National Natural Science Foundation of China (No. 61321492), National Natural Science Foundation of China under Grant Nos. 61176001, 51222211, 61274136, and 51322201, Specialized Research Fund for the Doctoral Program of Higher Education (No. 20120071110025), Science and Technology Commission of Shanghai Municipality (Nos. 12520706300 and 14JC1400200), and Chinese Academy of Sciences (CAS) International Collaboration and Innovation Program on High Mobility Materials Engineering.

- [1] D. Y. Khang, H. Q. Jiang, Y. Huang, J. A. Rogers, *Science* **2006**, *311*, 208.
- [2] L. Kranz, C. Gretener, J. Perrenoud, R. Schmitt, F. Pianezzi, F. L. Mattina, P. Blösch, E. Cheah, A. Chirilă, C. M. Fella, H. Hagendorfer, T. Jäger, S. Nishiwaki, A. R. Uhl, S. Buecheler, A. N. Tiwari, *Nat. Commun.* **2013**, *4*, 2306.
- [3] S. W. Hwang, H. Tao, D.-H. Kim, H. Cheng, J.-K. Song, E. Rill, M. A. Brenckle, B. Panilaitis, S. M. Won, Y.-S. Kim, Y. M. Song, K. J. Yu, A. Ameen, R. Li, Y. Su, M. Yang, D. L. Kaplan, M. R. Zakin, M. J. Slepian, Y. Huang, F. G. Omenetto, J. A. Rogers, *Science* **2012**, *337*, 1640.

- [4] G. H. Gelinck, H. E. A. Huitema, E. Veenendaal, E. Cantatore, L. Schrijnemakers, J. B. P. H. Putten, T. C. T. Geuns, M. Beenhakkers, J. B. Giesbers, B.-H. Huisman, E. J. Meijer, E. M. Benito, F. J. Touwslager, A. W. Marsman, B. J. E. Rens, D. M. Leeuw, *Nat. Mater.* **2004**, *3*, 106.
- [5] Y. Chen, H. Li, M. Li, *Sci. Rep.* **2012**, *2*, 622.
- [6] X. Wang, Y. Gu, Z. Xiong, Z. Cui, T. Zhang, *Adv. Mater.* **2014**, *26*, 1336.
- [7] G. Schwartz, B. C. -K. Tee, J. Mei, A. L. Appleton, D. H. Kim, H. Wang, Z. Bao, *Nat. Commun.* **2013**, *4*, 1859.
- [8] J. Lee, J. Wu, M. Shi, J. Yoon, S.-I. Park, M. Li, Z. Liu, Y. Huang, J. A. Rogers, *Adv. Mater.* **2011**, *23*, 986.
- [9] A. Nathan, B. Park, A. Sazonov, S. Tao, I. Chan, P. Servati, K. Karim, T. Charania, D. Striakhilev, Q. Ma, R. V. R. Murthy, *Microelectron. J.* **2000**, *31*, 883.
- [10] T. Sekitani, Y. Noguchi, K. Hata, T. Fukushima, T. Aida, T. Someya, *Science* **2008**, *321*, 1468.
- [11] A. Hara, F. Takeuchi, M. Takei, K. Suga, K. Yoshino, M. Chida, Y. Sano, N. Sasaki, *Jpn. J. Appl. Phys.* **2002**, *41*, 311.
- [12] M. Lee, Y. Jeon, T. Moon, S. Kim, *ACS Nano* **2011**, *5*, 2629.
- [13] J. R. Sánchez-Pérez, C. Boztug, F. Chen, F. F. Sudradjat, D. M. Paskiewicz, R. Jacobson, M. G. Lagally, R. Paiell, *Proc. Natl. Acad. Sci. U.S.A.* **2011**, *108*, 18893.
- [14] Y. Sun, W. M. Choi, H. Jiang, Y. Huang, J. A. Rogers, *Nat. Nanotechnol.* **2006**, *1*, 201.
- [15] Q. Guo, M. Zhang, Z. Xue, L. Ye, G. Wang, G. Huang, Y. Mei, X. Wang, Z. Di, *Appl. Phys. Lett.* **2013**, *103*, 264102.
- [16] M. Geissler, J. M. McLellan, Y. Xia, *Nano Lett.* **2005**, *5*, 31.
- [17] D. J. Lipomi, R. C. Chiechi, M. D. Dickey, G. M. Whitesides, *Nano Lett.* **2008**, *8*, 2100.
- [18] B. A. Ruben, B. J. F. Titulaer, E. Peeters, D. Burdinski, J. Huskens, H. J. W. Zandvliet, D. N. Reinhoudt, B. Poelsema, *Nano Lett.* **2006**, *6*, 1235.
- [19] K. Dietrich, D. Lehr, C. Helgert, A. Tünnermann, E.-B. Kley, *Adv. Mater.* **2012**, *24*, OP321.
- [20] M. Xue, Y. Yang, T. Cao, *Adv. Mater.* **2008**, *20*, 596.
- [21] O. Fakhri, P. Altpeter, K. Karrai, P. Lugli, *Small* **2011**, *7*, 2533.
- [22] Z. R. Dai, Z. W. Pan, Z. L. Wang, *Adv. Funct. Mater.* **2003**, *13*, 9.
- [23] A. Gao, N. Lu, P. Dai, T. Li, H. Pei, X. Gao, Y. Gong, Y. Wang, C. Fan, *Nano Lett.* **2011**, *11*, 3974.
- [24] J. A. Rogers, M. G. Lagally, R. G. Nuzzo, *Nature* **2011**, *477*, 45.
- [25] G. Huang, Y. Mei, *Adv. Mater.* **2012**, *24*, 2517.
- [26] A. P. Higginbotham, T. W. Larsen, J. Yao, H. Yan, C. M. Lieber, C. M. Marcus, F. Kuemmeth, *Nano Lett.* **2014**, *14*, 3582.
- [27] Q. Qing, Z. Jiang, L. Xu, R. Gao, L. Mai, C. M. Lieber, *Nat. Nanotechnol.* **2014**, *9*, 142.
- [28] A. J. Baca, J.-H. Ahn, Y. Sun, M. A. Meitl, E. Menard, H.-S. Kim, W. M. Choi, D.-H. Kim, Y. Huang, J. A. Rogers, *Angew. Chem. Int. Ed.* **2008**, *47*, 5524.
- [29] T. Someya, Y. Kato, T. Sekitani, S. Lba, Y. Noguchi, Y. Murase, H. Kawaguchi, T. Sakurai, *Proc. Natl. Acad. Sci. U.S.A.* **2005**, *102*, 12321.
- [30] N. A. Melosh, A. Boukai, F. Diana, B. Gerardot, A. Badolato, P. M. Petroff, J. R. Heath, *Science* **2003**, *300*, 112.
- [31] M. C. McAlpine, H. Ahmad, D. Wang, J. R. Heath, *Nat. Mater.* **2007**, *6*, 379.
- [32] H. C. Ko, A. J. Baca, J. A. Rogers, *Nano Lett.* **2006**, *6*, 2318.
- [33] R. Leancu, N. Moldovan, L. Csepregi, W. Lang, *Sens. Actuators, A* **1995**, *46*, 35.
- [34] M. A. Meitl, Z. Zhu, V. Kumar, K. J. Lee, X. Feng, Y. Huang, I. Adesida, R. G. Nuzzo, J. A. Rogers, *Nat. Mater.* **2006**, *5*, 33.
- [35] A. Carlson, A. M. Bowen, Y. Huang, R. G. Nuzzo, J. A. Rogers, *Adv. Mater.* **2012**, *24*, 5284.
- [36] H. Ko, K. Takei, R. Kapadia, S. Chuang, H. Fang, P. W. Leu, K. Ganapathi, E. Plis, H. S. Kim, S.-Y. Chen, M. Madsen, A. C. Ford, Y.-L. Chueh, S. Krishna, S. Salahuddin, A. Javey, *Nature* **2010**, *468*, 286.

- [37] J. Justice, C. Bower, M. Meitl, M. B. Mooney, M. A. Gubbins, B. Corbett, *Nat. Photon.* **2012**, *6*, 610.
- [38] H. Yang, D. Zhao, S. Chuwongin, J.-H. Seo, W. Yang, Y. Shuai, J. Berggren, M. Hammar, Z. Ma, W. Zhou, *Nat. Photon.* **2012**, *6*, 615.
- [39] J. A. Rogers, T. Someya, Y. Huang, *Science* **2010**, *327*, 1603.
- [40] X. Xu, H. Subbaraman, A. Hosseini, C.-Y. Lin, D. Kwong, R. T. Chen, *Opt. Lett.* **2012**, *37*, 1020.
- [41] J. Yao, H. Yan, C. M. Lieber, *Nat. Nanotechnol.* **2013**, *8*, 329.
- [42] A. Javey, S. Nam, R. S. Friedman, H. Yan, C. M. Lieber, *Nano Lett.* **2007**, *7*, 773.
- [43] K. J. Lee, M. J. Motala, M. A. Meitl, W. R. Childs, E. Menard, A. K. Shim, J. A. Rogers, R. G. Nuzzo, *Adv. Mater.* **2005**, *17*, 2332.
- [44] M. A. Meitl, X. Feng, J. Dong, E. Menard, P. M. Ferreira, Y. Huang, J. A. Rogers, *Appl. Phys. Lett.* **2007**, *90*, 083110.
- [45] Y. Yang, Y. Hwang, H. A. Cho, J.-H. Song, S.-J. Park, J. A. Rogers, H. C. Ko, *Small* **2011**, *7*, 484.
- [46] D. Jiang, X. Feng, B. Qu, Y. Wang, D. Fang, *Soft Matter* **2012**, *8*, 418.
- [47] J. M. Gere, B. J. Goodno, *Mechanics of Materials*, 7th ed., CL Engineering, Ludhiana, Punjab, India **2009**.
- [48] K. S. Novoselov, A. K. Geim, S. V. Morozov, D. Jiang, Y. Zhang, S. V. Dubonos, I. V. Grigorieva, A. A. Firsov, *Science* **2004**, *306*, 666.
- [49] T. Korhonen, P. Koskinen, *AIP Adv.* **2014**, *4*, 127125.
- [50] P. Koskinen, *J. Phys. Condens. Matter* **2013**, *25*, 395303.
- [51] A. A. Farajian, M. Mikami, *J. Phys. Condens. Matter* **2001**, *12*, 8049.
- [52] Properties of Silicon, INSPEC, Institution of Electrical Engineers, New York **1988**.
- [53] M. T. Kim, *Thin Solid Films* **1996**, *283*, 12.
- [54] T. L. Anderson, *Fracture Mechanics: Fundamentals and Applications*, CRC Press, Boca Raton, FL **1991**.
- [55] C. E. Inglis, *Trans. Inst. of Naval Architecture* **1913**, *55*, 219.
- [56] M. M. Roberts, L. J. Klein, D. E. Savage, K. A. Slinker, M. Friesen, G. Celler, M. A. Eriksson, M. G. Lagally, *Nat. Mater.* **2006**, *5*, 388.
- [57] S.-I. Park, J.-H. Ahn, X. Feng, S. Wang, Y. Huang, J. A. Rogers, *Adv. Funct. Mater.* **2008**, *18*, 2673.
- [58] P. Feng, I. Monch, G. Huang, S. Harazim, E. J. Smith, Y. Mei, O. G. Schmidt, *Adv. Mater.* **2010**, *22*, 3667.
- [59] P. Feng, I. Monch, S. Harazim, G. Huang, Y. Mei, O. G. Schmidt, *Nano Lett.* **2009**, *9*, 3453.
- [60] Y. Cui, C. M. Lieber, *Science* **2001**, *291*, 851.
- [61] X. Duan, Y. Huang, Y. Cui, J. Wang, C. M. Lieber, *Nature* **2001**, *409*, 66.
- [62] S. Chuang, R. Kapadia, H. Fang, T. C. Chang, W.-C. Yen, Y.-L. Chueh, A. Javey, *Appl. Phys. Lett.* **2013**, *102*, 242101.
- [63] A. M. Kiefer, D. M. Paskiewicz, A. M. Clausen, W. R. Buchwald, R. A. Soref, M. G. Lagally, *ACS Nano* **2011**, *2*, 1179.

Received: February 18, 2015

Revised: April 23, 2015

Published online: May 12, 2015